

1

2

3

4

5

6

7

8

9

10

11

12

13

14

15

16

17

18

19

20

21

22

23

24

25

26

27

28

29

30

31

32

33

34

35

36

37

38

39

40

41

42

43

44

45

46

47

48

49

50

51

52

53

54

55

56

57

58

59

60

Maskless Patterning of Metal Outflow in Alternating Metal/Ceramic
Multiple Nanolayers by Femtosecond Laser Irradiation

Luchan Lin^{1, 2}, Jinpeng Huo¹, Guisheng Zou¹, Lei Liu^{1*}, Lars P. H. Jeurgens², and Y. Norman Zhou³*

¹Department of Mechanical Engineering, Tsinghua University, Beijing100084, China
²Empa, Swiss Federal Laboratories for Materials Science and Technology, 8600 Dübendorf, Switzerland
³Center for Advanced Materials Joining, Department of Mechanical and Mechatronics Engineering, University of Waterloo, Waterloo, Ontario N2L 3G1, Canada

**Email: luchan.lin@empa.ch, liulei@tsinghua.edu.cn*

This document is the accepted manuscript version of the following article:
Lin, L., Huo, J., Zou, G., Liu, L., Jeurgens, L. P. H., & Zhou, Y. N. (2019). Maskless patterning of metal outflow in alternating metal/ceramic multiple nanolayers by femtosecond laser irradiation. Journal of Physical Chemistry C. <https://doi.org/10.1021/acs.jpcc.9b09884>

Abstract

In this work, solid-state metal transport from internal metal nanolayers onto the surface of metal/ceramic nano-multi-layers (NMLs) has been directed in a controlled way by femtosecond (fs) laser irradiation and subsequent low temperature thermal annealing. Laser irradiation induced modifications of the NML microstructures and stress states can be limited within the first few top nanolayers due to the focused laser energy input at the metal/ceramic interface by exploiting the local plasmonic effect. Accompanied laser peening can further refine the crystallites and introduce compressive stress at the laser-irradiated region, which reduces the activation energies for vacancy formation and migration of metal atoms in the nano-confinement. Patterned Cu surface nanostructures (outflow) appear selectively along the laser path after air annealing at temperatures down to 360 °C. For the solid-state diffusion of Cu in confinement, in-plane metal transport along the Cu-AlN interfaces is much faster than the outward short-circuit diffusion of Cu across the AlN barrier layers. Localized metal outflow is accompanied by the collapse and sintering of the remaining AlN barrier layers, under influence of the acting capillary forces, which may further accelerate the metal transport. This laser induced maskless patterning of metal outflow is not only applicable in Cu/AlN NMLs, but also in Ag/AlN NMLs, assisted by subsequent low temperature annealing.

1. Introduction

Heterogeneous metal/ceramic multi-layered structures have been widely used in electrical units or optical filters due to the high flexibility of the band diagram/permittivity adjustment.¹⁻³ With the continuing trend in device miniaturization down to the nanoscale, such functional nano-multi-layers (NMLs) become increasingly metastable and thereby more prone to degradation during application, which is a direct consequence of the increasing volume fraction of atoms associated with surfaces and interfaces. Actually, such size-dependent materials stabilities are known to be vital to the high performance and long-term service of a wide range of nanotechnologies. On the one hand, the intrinsically higher mobility of electrons (holes) and/or ions (ion vacancies) in the metastable nanostructured systems can be exploited for high performance electronic devices⁴ and device integration at lower temperatures.^{5,6} On the other hand, stable thin-films and multilayered microstructures can be utilized to achieve smooth optical/electrical response and extended device lifetimes.^{7,8} Fundamental understanding and engineering know-how of mass transport phenomena in metal/ceramic thin films and NMLs is needed to adjust their optical performances and electrical conductivities for photonics or electronics applications.

For a single metal thin film (nanolayer) on a ceramic substrate, solid state dewetting of the metal film can occur at temperatures far below the melting point, as governed by the chemistry and structure of the interface between the metal and the ceramic, as well as by the enhanced diffusivity of surface atoms. The dewetting of metallic nanolayers on ceramic substrates is generally driven by a minimization of the sum of surface and interface energies, and can result in the fast transformation of the metal layer into isolated particles (islands) at relative low temperatures.⁹⁻¹¹ When the metal nanolayer is confined on both sides by a ceramic layer, such as in a ceramic/metal/ceramic sandwich or respective NMLs, the metallic free surface will be replaced by

an additional metal-ceramic interface. The atomic mobility of metals in such nanoconfined systems will then depend on the chemistry and structure of the metal/ceramic interfaces and the resulting interface mobility only. For a highly coherent interface and strong chemical interaction between the metal and ceramic layers, the interfacial mobility of metal atoms can be suppressed, resulting in a superheating of the confined metal.¹² It is generally acknowledged that the atomic mobility and associated thermal stability may be greatly affected by the growth stresses and thermally-induced stresses in the metal layer.¹³⁻¹⁵ Notably, fast diffusion of metal atoms along incoherent and weakly bonded metal-ceramic interfaces can be surprisingly fast due to the relatively low activation energies of vacancy formation and migration in the metal.¹⁶ Hence, depending on the nature of the metal-ceramic interface and the residual stress state, the microstructural response of metal nanolayers upon thermal/mechanical post-treatment can be distinctly different between confined and non-confined metal-ceramic nanolaminates.

Thermal destabilization of nano-confined metal nanolayers is not only associated with fast in-plane mass transport of the confined metal atoms along internal interfaces, but can also result in fast out-of-plane transport of the confined metal across the ceramic barrier to the free surface, as accompanied by the relaxation of residual stresses in the structures. As a result, large metal protrusions (designated as *metal outflow*) can develop on the free barrier surface upon thermal annealing, which leaves porosity and/or voids in the remaining nanolayered structures.¹⁷⁻²⁰ Such fast metal outward transport during annealing strongly depends on the deposition stress and the as-deposited microstructures (e.g. grain size, texture, interface coherency, defect structure) of the studied nanolayer system.²⁰ Unfortunately, it is still an ultimate engineering challenge to tune the deposition conditions of physical vapor deposition techniques, such to obtain a homogenous/designed microstructure and stress state of the metal and ceramic nanostructures at the nanoscale. Typically, highly anisotropic microstructures and local stress gradients occur in the

as-deposited nanolaminated structures, especially in alternating metal/ceramic NMLs. Consequently, thermally activated metal outflow upon thermal treatment of such heterogeneous NML microstructures results in randomized metal outflow onto the free surface.

In-plane diffusion along metal-ceramic interfaces and outward diffusion via short circuits, such as grain boundaries and/or cracks in the ceramic barrier layers, constitute the principle metal transport processes for realizing fast metal outflow in confined nanolayered systems. The metal-ceramic interface state and the residual stress gradients will be decisive in enhancing and directing fast mass transport once thermally activated. It is known that local variations of the interface state and the stress gradient can effectively affect the local atomic mobilities in the structure.^{21, 22} Hence, engineered interface structures and stress gradients in NMLs can be intentionally applied by e.g. nanoindentation to reduce the associated kinetic barriers for atomic mass transport at the local scale.²³ As such, fast mass transport upon annealing can be triggered to occur selectively at specific sites in the NML structure only. However, such local modifications of the NML structure by externally applied mechanical forces need precise and homogeneous dosing of the deformation energy, which is obstructed by the intrinsic heterogeneous microstructure. Alternatively, laser irradiation could be applied for locally altering as-deposited metallic nanostructures, which provides an easier and more accurate control of the dose and spatial distribution of external energy input into the nanostructure.²⁴ In particular, heterogeneous metal/ceramic (i.e. metal-dielectric) structures and their interfaces can be precisely modified using laser irradiation by exploiting the so-called localized plasmonic effect to locally deposit the laser energy.²⁵⁻²⁷ In addition, laser peening between a transparent dielectric (e.g. air or ceramic) and a metal can invoke strong and localized compressive stresses in the nanostructure, which could be exploited to tailor local stress gradients.

28, 29

In this work, we demonstrate the precise and local engineering of microstructures and stress states in metal/ceramic NMLs (Cu/AlN and Ag/AlN) by highly focused fs laser irradiation, to achieve fast patterned outflow of the confined metal to the free surface upon subsequent short-time (5 min) annealing. The NML microstructures prior to and after laser irradiation, as well as before and after thermal annealing, were studied in detail by scanning electron microscopy (SEM) and high resolution transmission electron microscopy (HRTEM). As such, the underlying driving forces and mechanisms for fast directional mass transport in the modified regions of the annealed metal/ceramic NMLs, as generated by laser induced plasmonic interface modifications and the peening effect, are disclosed. This maskless patterning approach can be promising for fast surface nanostructures fabrication for optical and electrical applications, such as nanoscale optical gratings and electrical heaters.

2. Experiments

The metal/ceramic NMLs were deposited on sapphire substrates (α -Al₂O₃, (0001)) using magnetron sputtering at room temperature. A 10 nm thick AlN nanolayer was firstly pre-deposited on the sapphire substrate, acting as a buffer layer. Next, metal (Cu or Ag) and ceramic (AlN) nanolayers with individual layer thicknesses of 5 nm were alternatively sputtered to obtain a NML structure. The metal-ceramic bilayer repetition was fixed at 10. The detailed deposition process is reported in refs. [18, 30].

A Ti: sapphire ultrafast laser system was used to generate 35 fs, 800 nm laser pulses. A couple of reflective mirrors and neutral filter lens were used to attenuate the energy of the laser beam down to a few milli-Watt. The laser beam was then compressed, aligned and introduced in an Olympus Optical microscope (Olympus BX51). An objective lens (NA0.5, 50 \times) and high precision moving platform (V31XYZ ProScan III) were used to control the beam size on the NML sample surface.

The laser beam was blocked by an electrically controlled shutter to control the laser irradiation time.

After laser irradiation, the laser-treated NML samples were transferred to a tubular furnace and annealed in air. The annealing treatment at a given temperature was performed with a ramping rate of 20 K/min and holding time of 5 min. After the annealing, the samples were cooled down freely within the furnace. Scanning electron microscopy (SEM, Zeiss Supra 55) was used to characterize the surface structures of the annealed NMLs. Focused ion beam (FIB, FEI Helios 660) was used to prepare the cross sections at selected regions, as well as to prepare TEM lamellas. A transmission electron microscope (TEM, JEOL2200FS), operated at 200 kV and equipped with EDX and HAADF detectors, was used to characterize the microstructures of as-prepared lamella.

The plasmonic effect induced electric field intensity in metal/ceramic NML in response to the incident laser beam was simulated using a commercial finite element method simulation software (COMSOL Multiphysics, 4.3b) with an RF module. The incident laser wavelength was 800 nm with a polarization direction parallel to the substrate. Physical parameters of the studied metal (Cu) and ceramic (AlN) materials under given laser conditions were adapted from refs. [31] and [32], respectively.

3. Results

3.1 Surface structures of thermal annealed NMLs

Figure 1 shows the surface structures of the as-deposited metal/ceramic (Cu/AlN) NMLs on sapphire, indicating a smooth surface with a roughness in the range of 0.5 nm. The cross-sectional images in figure S1(a) show the alternating 5 nm thick Cu and AlN nanolayers (10 repetitions) on top of the 10 nm thick AlN buffer layer and the underlying sapphire substrate (designated as $[\text{Cu}_{5\text{nm}}/\text{AlN}_{5\text{nm}}]*10$). The internal nanolayers are intact and the interface roughness is within a few

1
2
3 nanometers. The metal and ceramic nanolayers possess a polycrystalline nature, consisting of tiny
4
5 nanocrystallites. Magnified TEM imaging of the metal-ceramic interface indicates that the Cu(200)
6
7 lattice planes are typically parallel to the AlN(002) planes, resulting in an in-plane texture (figure
8
9 S1(b)).
10

11
12
13 After thermal annealing at 400 °C for 30 min in air, few nanoparticles are randomly distributed on
14
15 the annealed NML surface (figure 1(c)). Different local microstructures can be observed around
16
17 smaller and bigger surface particles, which result from local differences in the redistribution of
18
19 confined Cu metal by in-plane and out-of-plane diffusion during the annealing process.²⁰
20
21 Compared with the as-deposited NMLs, Cu has a much higher concentration at the particle location
22
23 after the annealing (Zone 2 in figure S2), indicating that some Cu has migrated to the free surface
24
25 and formed tiny surface structures (i.e. outflow). It is generally recognized that confined metals can
26
27 diffuse along internal interfaces, such as phase and grain boundaries, at temperature much below
28
29 the bulk melting point. The atomic mobility of the confined metal and the associated redistribution
30
31 of Cu upon annealing will vary locally, depending on the local defect structure. More defective
32
33 regions will exhibit an enhanced atomic mobility and associated materials redistribution towards
34
35 lower temperatures.²³ Due to the heterogeneous microstructure and associated local variations of
36
37 the stress state in the as deposited NMLs, thermally activated metal outflow will occur randomly
38
39 at more defective sites (with a higher Gibbs energy) within the NMLs. At an annealing temperature
40
41 of 400 °C, the atomic mobility is still kinetically frozen in most regions of the as deposited
42
43 microstructure, and hence only a few Cu particles form on the surface. Only when the annealing
44
45 temperature is increased to 500 °C, the atomic mobility is thermally activated over the entire as-
46
47 deposited microstructure, resulting in massive and randomized Cu outflow on the entire NML
48
49 surface (figure 1(d)).
50
51
52
53
54
55
56
57
58
59
60

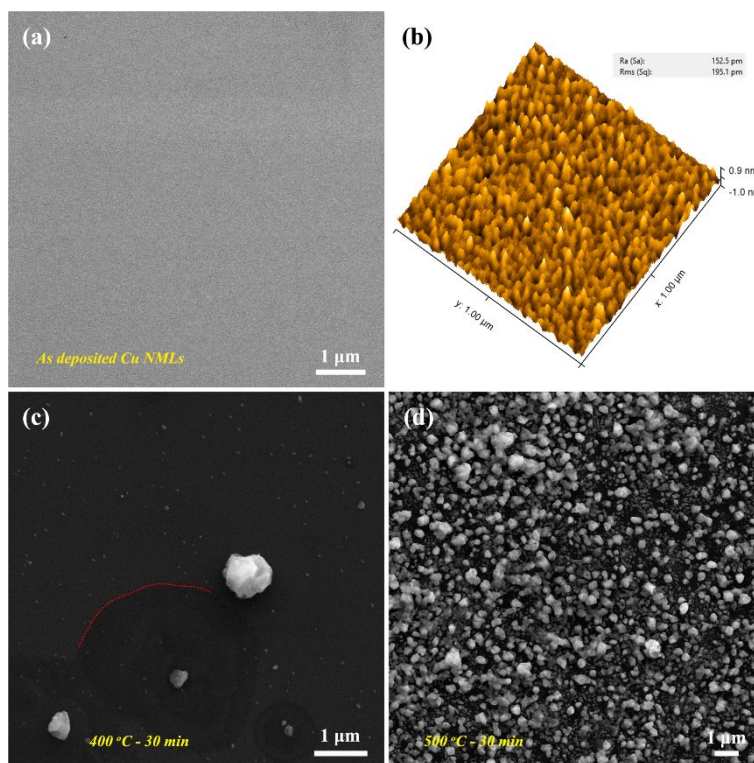


Figure 1. Surface structures of as deposited and thermally annealed $[\text{Cu}_{5\text{nm}}/\text{AlN}_{5\text{nm}}]*10$ NMLs. SEM images of (a) as deposited and thermally annealed NMLs at (c) 400 °C and (d) 500 °C for 30 min in air. (b) AFM topography of as deposited NMLs. Inset in (b) shows the surface roughness of the NML. The dashed line in (c) indicates the boundary of local contrast difference in the SEM image.

3.2 Surface structures of laser irradiated NMLs after subsequent annealing

Figure 2 shows the surface structures of the NMLs after laser irradiation and subsequent thermal annealing. Line shaped surface structures have formed at lower temperatures and within shorter times (~ 360 °C, 5 min) in the laser-irradiated zone, as compared to the untreated NML regions. Away from the line structures, only very few surface nanoparticles can be observed. At low laser scanning speed, the incident energy can be high enough to ablate the NMLs, resulting in the formation of an open trench in the NML. Subsequent annealing results in the thermally activated (in-plane) diffusion of Cu to those trench edges, which partially fills the gap. However, for short annealing times at low temperatures, the diffusion length of Cu is only limited and, consequently,

only a limited amount of Cu can be transported to the trench during the annealing process. The trench edges are therefore decorated with a Cu nanowires pair on opposite sides, separated by a gap (figure 2(a)). The microstructural modifications in the NML can be easily and well controlled by increasing the scanning speed, which also minimizes the degree of materials ablation. As such, the surface structures as formed by Cu outflow can be changed from an interwoven network to a straight wire and even interconnected filaments (figures 2(b)-2(d)). Importantly, all surface structures are selectively formed along the laser paths only. This indicates that the defect structure in the NMLs has been locally modified, resulting in an enhanced atomic mobility towards lower temperatures, which is only limited to the laser irradiated regions. Thus, fast mass transport of internal metals to the surface upon annealing can be selectively directed along the laser path by tuning the laser irradiation conditions, even for short annealing times at relatively low temperatures.

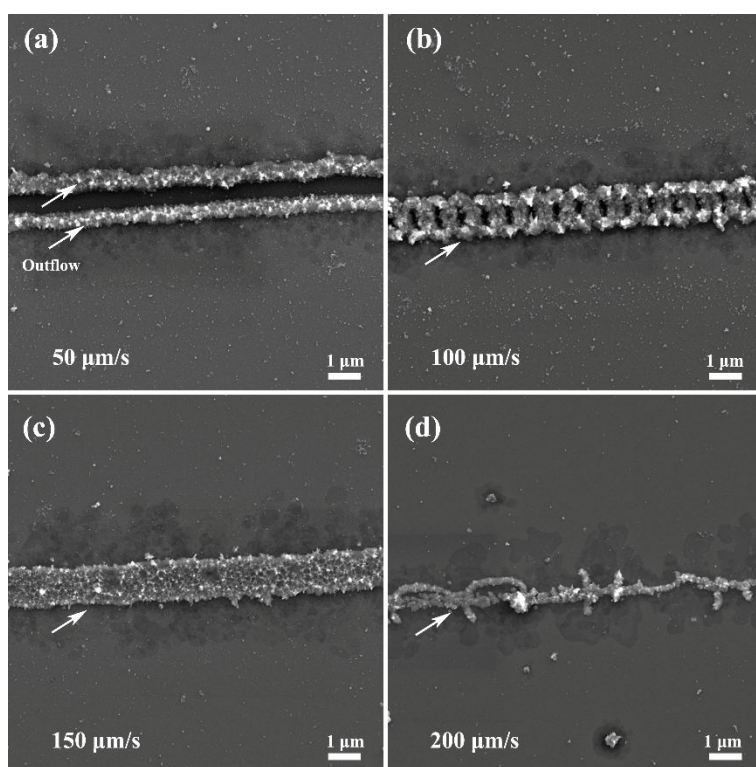


Figure 2. Surface structures formed on $[\text{Cu}_{5\text{nm}}/\text{AlN}_{5\text{nm}}]*10$ NMLs after laser irradiation and subsequent thermal annealing. Laser scanning speed: (a) $50\text{ }\mu\text{m/s}$, (b) $100\text{ }\mu\text{m/s}$, (c) $150\text{ }\mu\text{m/s}$, and (d) $200\text{ }\mu\text{m/s}$. Laser

fluence: $\sim 90 \text{ J/cm}^2$. Annealing temperature: 360°C . Holding time: 5 min. Arrows indicate the surface nanostructures (outflow) after thermal annealing.

By slightly increasing the annealing temperature to 400°C , more confined Cu will migrate to the surface, which results in an improved structural uniformity (figure 3). Due to internal materials redistribution, similar localized contrast differences in the image (shown in figure 1(c)) appear in the laser treated NML within limited distances after thermal annealing, as sketched in figure 3. It should be noted that oxidation of the formed surface nanostructure can occur when Cu metal migrates to the surface during the annealing process in air, resulting in Kirkendall voiding of the Cu nanostructures.^{33,34} Hollow nanostructures can thus be formed due to the surface oxidation and associated fast grain boundary diffusion of Cu across the initial oxide film to the free surface. Indeed, in the laser-irradiated and annealed Cu/AlN NMLs, voids can be observed within the surface wire structures (insets in figure 3). These Kirkendall voids are much smaller if the surface wire is narrower. As shown in figure 3(b), if the wire width is $\sim 500 \text{ nm}$, inner voids only constitute $\sim 6\%$ of the cross section.

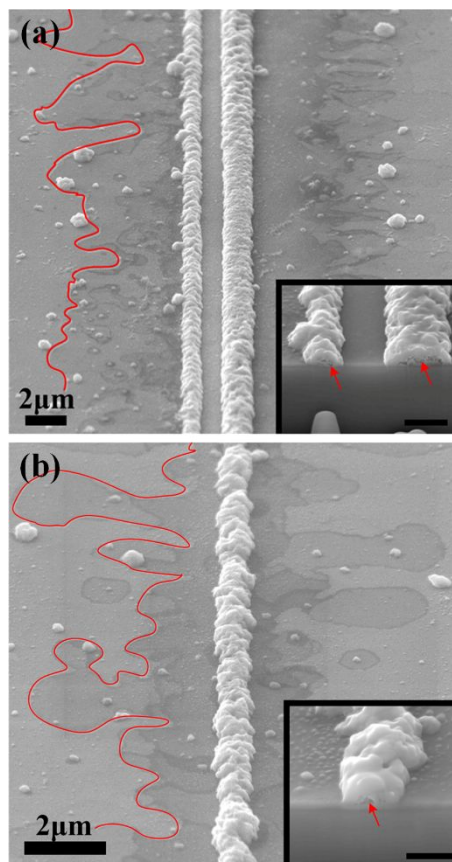


Figure 3. Surface and cross sectional structures of $[\text{Cu}_{5\text{nm}}/\text{AlN}_{5\text{nm}}]*10$ NMLs after laser irradiation and subsequent thermal annealing. Laser fluence: (a) $\sim 55 \text{ J/cm}^2$ and (b) $\sim 33 \text{ J/cm}^2$. Scanning speed: $50 \text{ } \mu\text{m/s}$. Annealing temperature: $400 \text{ }^\circ\text{C}$. Holding time: 5 min. Red lines sketch the dark contrast regions adjacent to the wires structures. Inset scale bars: (a) $1 \text{ } \mu\text{m}$, (b) 500 nm . Title angle: 45° . Red arrows show the voids in the formed surface structures.

3.3 Internal structures of laser irradiated NMLs after subsequent annealing

To clarify the underlying mechanisms for selective metal outflow within the laser-processed regions at reduced annealing temperatures, a TEM lamella was prepared by FIB perpendicular to the laser path direction and analyzed by TEM. Figure 4 shows cross sectional STEM images of the wire-shaped surface structure, as fabricated by laser irradiation and subsequent annealing. The application of high intensity fs laser irradiation can induce modifications throughout the entire NML stack (i.e. from the surface to the bottom). As shown in figure 4(b), $\sim 35\%$ of the cross section

of the wire with a width of $\sim 1\ \mu\text{m}$ is constituted of void, which originates from oxidation-induced Kirkendall voiding. Therefore, the surface nanostructure is a mixture of metal and surficial Cu oxides (figure S3). It shows that the hollow wire stands on the top AlN layer and is isolated from the remaining Cu nanolayers underneath. Within the dark contrast region in the NML adjacent to the Cu wire in figure 4(a), internal Cu has been relocated from the first few top nanolayers to the NML surface (indicated by the red arrows). This indicates that in-plane mass transport of Cu from adjacent regions to the laser-irradiated path (with a diffusion length of 10-15 times the Cu wire width) also contributes to Cu wire formation upon annealing. The supplied Cu for surface structure formation does not only come from the top Cu nanolayers in the NML stack, but can also be supplied from deeper nanolayers (figure 4(c)), and even from the bottom metal nanolayer (figure 4(e)). For short time annealing at 400°C , the average length for short circuit diffusion of Cu through AlN and Cu grain boundaries is limited. Strikingly, after the annealing, the original NML sequence is better preserved directly below the surface wire structure (~ 7 layers left, figure 4(d)) than adjacent to it (5 layers, figure 4(c) and 4(e)). This may be attributed to the combined laser thermal/mechanical effects, which result in a complex defective structure around the laser irradiation zone (see Sec. 4).

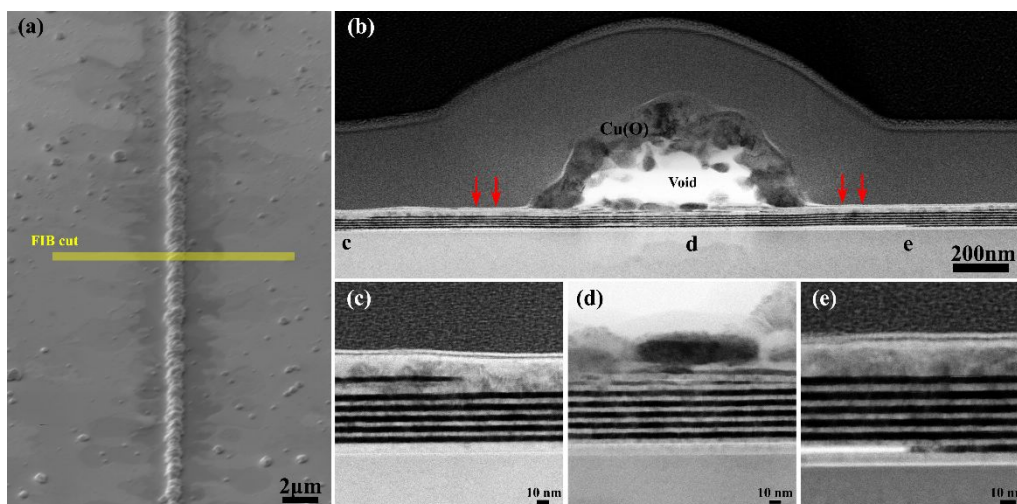


Figure 4. (a) SEM and (b)-(e) BF-STEM images of fs laser irradiated $[\text{Cu}_{5\text{nm}}/\text{AlN}_{5\text{nm}}]*10$ NMLs after thermal annealing at 400 °C for 5 min in air. Laser fluence: $\sim 40 \text{ J/cm}^2$. Scanning speed: $50 \text{ }\mu\text{m/s}$.

Figure 5 shows the HRTEM images of the interface region between the Cu surface wire and the top nanolayers of the NML stack in figure 4(b). The Cu surface structure has formed a dense interface with AlN, although a high density of defects and a few voids are present along the interface (red dash, figure 5(a)). Strikingly, the remaining AlN layers after Cu outflow are sintered together, resulting in a thicker AlN barrier layer (i.e. layer thickness much larger than the as-deposited 5 nm nanolayer). Inside the sintered AlN nanolayer, few tiny Cu crystallites can still be observed. Since the annealing was conducted for short times at temperatures much lower than the bulk melting point, the surface wire should be formed by a fast solid-state diffusion process. Due to a partial oxidation of the Cu surface structure, a fine-grained polycrystalline structure with associated Moiré planes can be observed, indicating a large amount of overlapping lattice planes along the beam direction in the surface structure (figure 5(b)). An irregular "zig-zag" interface is formed between the surface wire and the underlying AlN layer, which can be ascribed to interface energy minimization.³⁵ Along with the sintered AlN layers, the interface roughness between the remaining fragments of the Cu nanolayer and AlN nanolayer is increased after the annealing, especially on the bottom side (figure 5(d)). Notably, the scale of the interfacial zig-zag patterns is of the same order as the columnar AlN nanograin size and the respective nanolayer thickness. This suggests that the outward transport of Cu with concurrent "zipping" of the confining AlN layer is accompanied by tiny reorientations of the nano-sized grains in AlN barrier layers to increase the interface coherency at the underlying Cu/AlN interfaces, thereby reducing the system's energy. Consequently, the sintered AlN nanolayers do not show any distinct crystallographic planes constituted of high-angle (high energetic) grain boundaries, which contributes to a reduction of the system's energy (figure 5(c)).

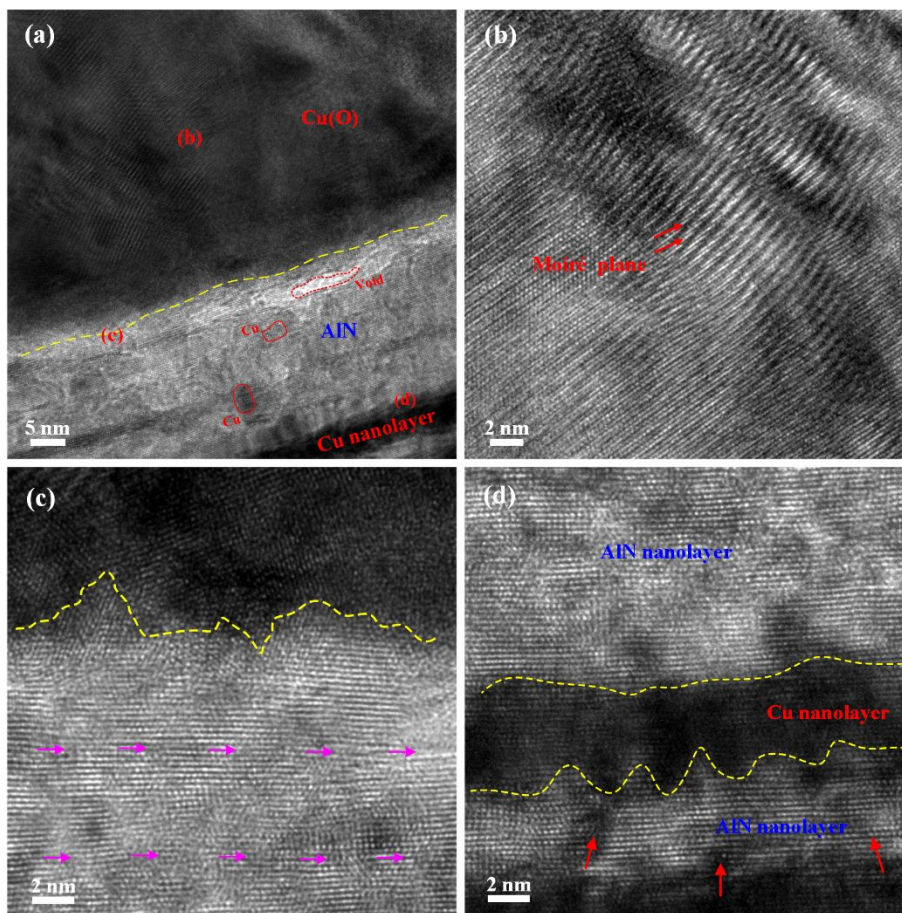


Figure 5. (a) Cross sectional TEM images of the fabricated surface wire on the Cu/AlN NML as indicated in figure 4(b). Yellow dashed lines sketch the Cu-AlN interfaces. HRTEM images of (b) the fabricated surface nanostructure, (c) interfacial state between the surface nanostructure and the NML, and (d) NML after metal migration on the top layers. Pink single arrows in (c) show the estimated boundaries between the as deposited 5 nm AlN nanolayers. Red arrows in (d) show the penetrated Cu in AlN layers.

A more localized and tuned microstructural modification of the NML structure can be realized for lower laser energy inputs. Figure 6 shows the surface structure formed after laser irradiation at a scanning speed of 300 $\mu\text{m/s}$ and subsequent thermal annealing at 400 $^{\circ}\text{C}$ for 5 min. A wire structure is not formed, but rather material has been redistributed internally along the laser path, as partially sketched in figure 6(a). Only a few larger nanoparticles due to Cu outflow appear locally along the laser-irradiated path. As shown in figure 6(b), only the first Cu nanolayer on the top disappears

after thermal annealing with 9 intact Cu/AlN repetitions remaining underneath. It should be noted that Cu nanoparticles can also be observed at locations where the NMLs is still intact (10 repetitions), which suggest fast in-plane mass transport of Cu along Cu/AlN interfaces and/or on top of the AlN surface to these specific locations. The outward migration of Cu from the first nanolayer is also accompanied by a "zipping" and subsequent sintering of the confining AlN barrier layers (figure 6(c)). EDX line scans along the dashed line in (c) show the corresponding elemental depth distribution, evidencing 9 Cu/AlN repetitions, as also observed in other locations (Figure S4). As a result, the nanoparticle stands on two tightly sintered AlN layers (figure 6(d)). The oxygen concentration in the confined Cu nanolayers after annealing the NML in air is relatively low and constant as a function of depth below the surface, which indicates that the internal NML structure is not severely degraded by thermal oxidation. It can be concluded that laser irradiation induced microstructural modification of the NML can be precisely tuned down to a single nanolayer, while keeping the rest of the NML structure intact. By well controlling the depth of the laser-affected zone, Cu from the first confined metal nanolayer can be selectively transported to the free surface at the laser-irradiated location at relatively low annealing temperatures.

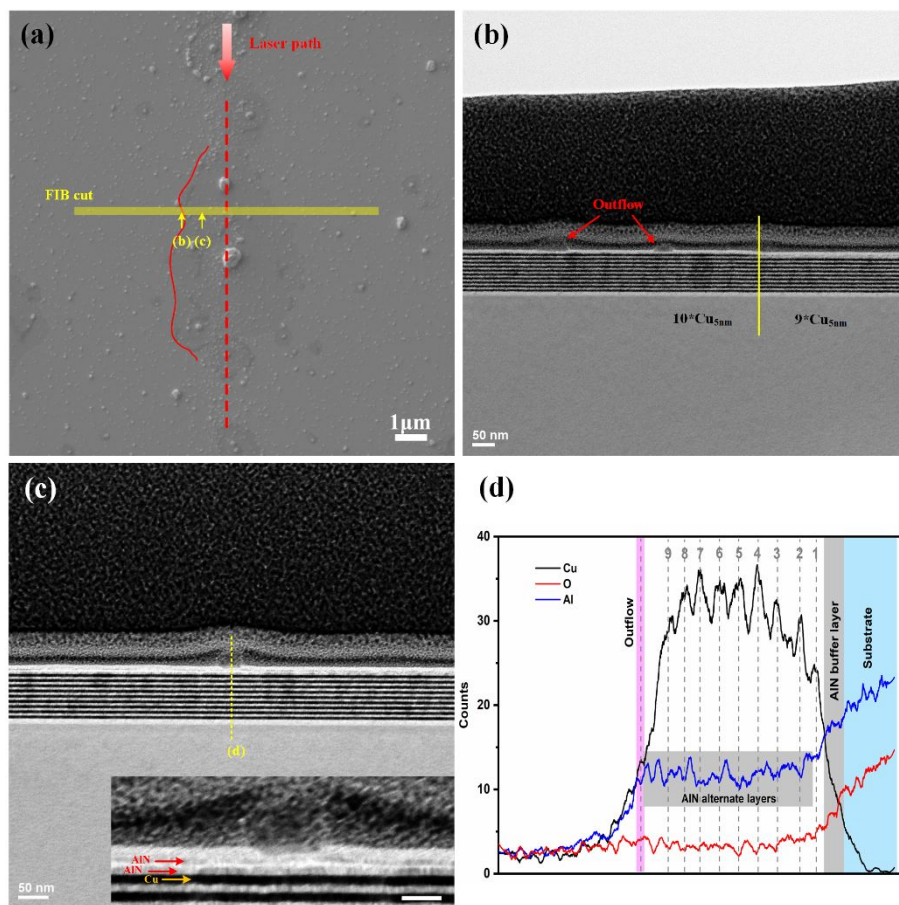


Figure 6. (a) SEM and (b, c) BF-STEM images of fs laser irradiated $[\text{Cu}_{5\text{nm}}/\text{AlN}_{5\text{nm}}]*10$ NMLs after thermal annealing at 400 °C for 5 min in air. (d): EDX elements distribution along the dash line in (c). Laser fluence: $\sim 33 \text{ J/cm}^2$. Scanning speed: 500 $\mu\text{m/s}$. Insets scale bar in (c): 20 nm.

Figure 7 shows the structure of the Cu/AlN interfaces after partial metal outflow from the top Cu nanolayer. In the transition region between the AlN layers and the remaining Cu nanolayer fragment, the surface AlN nanolayer is bend and exhibits a high defect density at its interface with the underlying Cu nanolayer (figure 7(a)). It is known that the interface coherency in chemically inert metal/ceramic NML systems is generally improved upon annealing.¹⁸ An increased interface coherency generally results in increased activation energies for vacancy formation and migration within the confined metal layer at the metal/ceramic interface.^{23, 36} For the annealing of the Cu/AlN NML at 400 °C, confined Cu metal in regions far away from the laser irradiated affected regions

will be less defective and therefore have a much lower atomic mobility, thus preserving its confinement after low temperature annealing. Similarly, the boundary plane (B1) between the sintered AlN nanolayers can hardly be observed, whereas the metal/ceramic boundaries directly underneath (B2 and B3) have a large roughness (figure 7(b)). Although laser peening may occur to modify the NML microstructure towards larger depths, cross sectional HRTEM analysis indicates that the nanolayers at the bottom and middle of the NML still have a similar microstructure as the as-deposited NML (figures 7(c) and 7(d)).

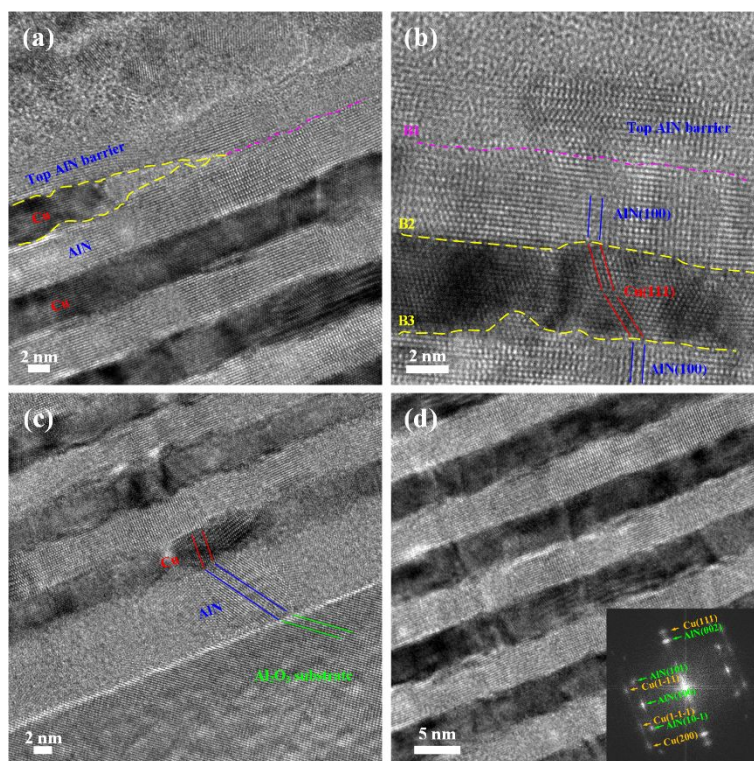


Figure 7. Cross sectional TEM images of laser irradiated $[Cu_{5nm}/AlN_{5nm}] \times 10$ NMLs after thermal annealing at 400 °C for 5 min in air. (a)(b): Top. (c): Bottom and (d): Middle.

It may be assumed that tailored modification of metal/ceramic NMLs for directional outflow due to laser-induced thermal and peening effects is applicable to other materials combinations. Indeed, as observed in the present study, selective Ag surface structures along laser paths can also be fabricated by laser irradiation and subsequent annealing of Ag/AlN NMLs (figure 8). When a low

laser irradiation energy is applied, Ag nanoparticles come out separately along the laser path after thermal annealing at 450 °C for 5 min. More extensive localized Ag outflow can be achieved by increasing the incident laser energy. Since the stress state in Ag microstructures can significantly accelerate Ag transport or even facilitate whisker growth,³⁷ surface nanostructure formation varies strongly with the laser conditions. Still, directional Ag outflow in NML following the laser paths/patterns can be achieved by fs laser irradiation and annealing processes.

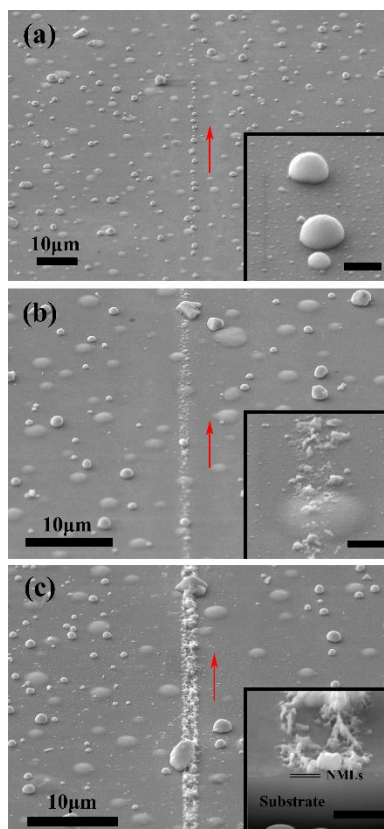


Figure 8. Surface structures of laser irradiated $[\text{Ag}_{5\text{nm}}/\text{AlN}_{5\text{nm}}]*10$ NMLs after subsequent thermal annealing. Scanning speed: (a) 500 $\mu\text{m/s}$, (b) 300 $\mu\text{m/s}$ and (c) 200 $\mu\text{m/s}$. Laser fluence: $\sim 33 \text{ J/cm}^2$. Temperature: 450 °C. Duration: 5 min. Atmosphere: air. Tilt angle: 45°. Inset scale bar: 1 μm .

4. Discussion

4.1 Laser peening effects on NML

The stress state in as deposited thin films can greatly affect the atomic mobility and thereby its thermal stability.¹⁵ During the initial stages of thin film growth, a tensile stress contribution is generated as a result of grain coalescence, while a compressive stress is generated during the post-coalescence stage.³⁸ Thermally activated diffusion of metal atoms in thin films or confined nanolayers can be directed along local (in-plane or out-of-plane) stress gradients in nanolaminated structures.²⁰ In particular, compressive residual stresses in nanoscale metal/ceramic NMLs can facilitate directional metal outward transport during annealing.¹⁸

It is known that compressive residual stress can be generated in metals (or alloys) substrate, when high energy laser pulses are introduced on the substrate with a transparent buffer layer on top.²⁹ The estimated surface residual stress when irradiated with a round laser spot is calculated as:^{28, 39}

$$\sigma_{\text{surf}} = \sigma_0 - [\mu \varepsilon_p (1 + \nu) / (1 - \nu) + \sigma_0] \left[1 - \frac{4\sqrt{2}}{\pi} (1 + \nu) \frac{L_p}{r_p \sqrt{2}} \right] \quad (1)$$

Where σ_0 is the initial residual stress (constant) and ν is Possion's ratio. r_p is the radius of laser spot. L_p is the plastically affected depth. ε_p is the surface plastic strain. μ is the Lamé's constant.

The plastically affected depth (L_p) can be calculated as,

$$L_p = \frac{C_e C_p \tau P}{C_e - C_p 2P_H} \quad (2)$$

Where C_e and C_p are the elastic and plastic shock wave velocities, respectively. τ is the pulse duration. P and P_H are the laser peak pressure and metal dynamic yield strength, respectively.

In metal/ceramic NMLs, the top metallic nanolayer (e.g. Cu or Ag) is covered by a ceramic (AlN) barrier layer, which can act as the transparent buffer layer during laser irradiation. With the introduction of high intensity fs laser pulses (below the ablation threshold of materials), laser peening can occur which introduces residual stresses in the confined metal nanolayers and also

generate dislocations.^{40, 41} Since the laser pulse duration here is only 35 fs, the plastically affected depth can be extremely small (e.g. L_p will be 10^{-6} of that using a 3.5 ns laser pulse with a similar peak pressure). However, for layer thicknesses in the range of 5 nm, as for the studied Cu/AlN NMLs, the entire depth of the NML can be affected by such short laser pulses irradiation.

Apart from mechanical peening, thermo-mechanical effects may occur in nanolaminated systems, which can weaken the film-film interface. On this basis, nanolayers can even be precisely peeled off layer by layer from the structure using fs laser irradiation.²⁷ At metal/ceramic interfaces, a rarefaction wave accompanied with the thermal wave will be produced due to the laser thermal effect. Those waves can penetrate into the sample and cause rupture at the boundary of nanolayers, further weakening the interface bond between metal and ceramic nanolayers.

4.2 Plasmonic effect at metal-ceramic interface

The plasmonic effect can occur at the metal-dielectric interface under optical excitation, which can redistribute the incident energy and bring in localized 'hot spots' for precise interface engineering.^{25, 26, 42} In Cu/AlN (i.e. metal/dielectric) NMLs, plasmons can be excited along the metal-ceramic interface. Figure 9 shows the simulation result of the electric field distribution under focused optical excitation, where an enhanced electric field can penetrate through the metal barriers to lower layers and propagate to the region outside laser irradiated zone within a certain distance. The field intensity distribution in the vertical direction will be affected by the multiple layer structures, while in the horizontal direction, it will be mainly determined by the first metal and ceramic layers (Supplementary note). Since the excitation of coherent oscillations of electrons via plasmon resonance can locally change the electromagnetic fields, the generated field intensity can be further enhanced by high-energy (e.g. fs) laser pulse excitation, resulting in strong nonlinear photons absorption effect.⁴³ These incident photons will mainly be absorbed by the top ceramic and

underlying metal nanolayers, while the deeper nanolayers will be mostly affected by the resulting thermal conduction from the top nanolayers. Thus, intense energy from the laser pulses will mainly be introduced into the first few top Cu/AlN nanolayers.

Meanwhile, intense photons absorption under strong electromagnetic field can generate fierce lattice resonance. Massive instabilities in the crystal lattice can occur under rapid excitation of electrons due to a perturbation of the interatomic bonds.⁴⁴ With low energy input, a bond weakening can be expected in the topmost AlN layer. Since the melting point depression can be significant for metal layer thickness down to ~ 5 nm, subsequent pre-melting may occur in the top Cu nanolayer. Due to the short laser pulse duration (35 fs), other fast non-equilibrium thermal processes can also happen in the Cu nanolayers.⁴⁵ For example, intense laser pulse irradiation on material has been reported to induce intermixing, grain refinement, and phase transformation or dissociation.⁴⁶⁻⁴⁸ Since the size of the as deposited metal (ceramic) crystallites is in the nanoscale (figure S1), a laser induced grain refinement effect may be difficult to observe. However, the (point/line) defect density in both the metal and ceramic layers could be enhanced. Accordingly, interface structures and orientation relationship can be adjusted locally, which can directly affect the local activation energies for the vacancy formation and migration, and thereby the diffusion rates.

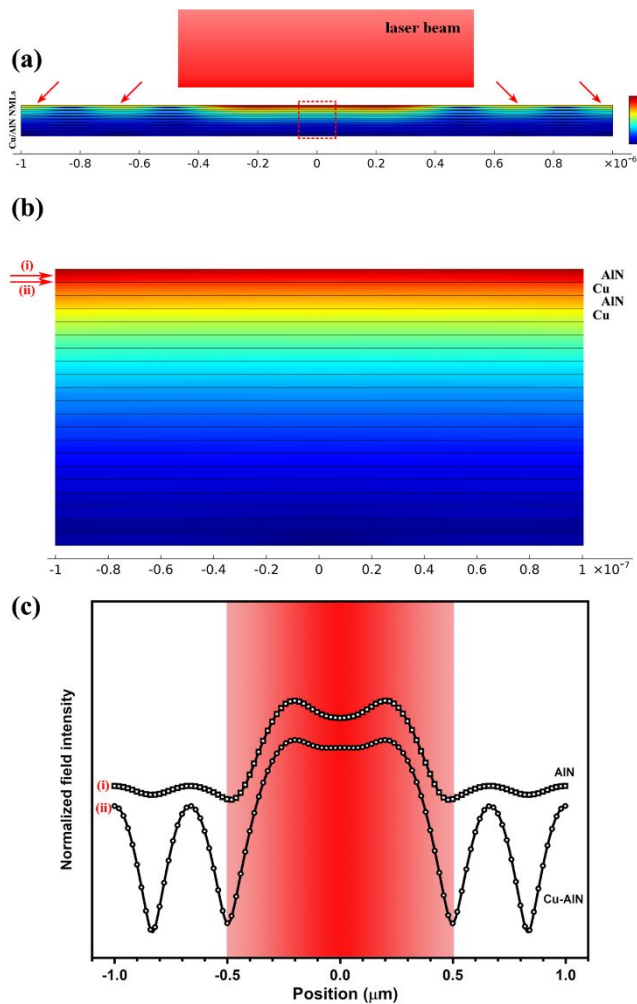


Figure 9. Simulated electric field intensity distribution in [Cu/AlN]*10 NMLs. (a) Field distribution in and out of laser irradiated region. Arrows show the locations with enhanced field intensity outside the laser irradiated region. (b) Field intensity distribution in the rectangle zone in (a). (c) Normalized field intensity along the first AlN layer and Cu-AlN interface on the top. Incident laser beam diameter is 1 μm .

4.3 Directional fast mass transport

It is known that metal outflow in metal/ceramic NMLs is the result of the delicate interplay between temperature, microstructure, stress and processing atmosphere.¹⁸ Interfacial pre-melting will be suppressed for highly coherent (less-defective) intercrystalline interfaces. The intrinsically high density of grain boundaries in the studied Cu/AlN NML can also contribute to a melting point

depression. Furthermore, the activation energies for vacancy formation and migration in metal nanolayers in contact with ceramics can be significantly lower as compared to the respective bulk metal, in particular if the metal only weakly wets or does not wet the ceramic.¹⁶ The above effects can all contribute to a very fast diffusion of confined metals in metal/ceramic NMLs upon heating. Our experimental findings show that the atomic mobility of Cu in the as-deposited Cu/AlN NML is still kinetically hindered in most microstructural regions when annealed at temperatures up to 400 °C. Metal outflow preferentially occurs only at local sites with a high Gibbs energy, as mainly determined by the local microstructures (e.g. interface coherency, defects) and the stress state. Laser irradiation can induce localized compressive stress gradients and defective zones in the NML structure, which effectively reduce the activation energies for short-circuit diffusion of Cu in the confinement. Hence, annealing of the laser-irradiated NMLs at temperatures lower than 400 °C can thermally activate fast directional outflow of Cu metal to the free surface selectively at the laser affected regions. Such fast Cu metal outflow is accompanied by a "zipping" and subsequent sintering of the AlN barriers, which is presumably aided by capillary forces, striving for a minimization of the participating interface energies. Metal in-plane transport along the interface and outward transport across AlN barrier can be facilitated by capillary forces until the barriers sinter together. Therefore, directional metal outflow in Cu/AlN and Ag/AlN NMLs for maskless surface structure patterning using laser irradiation can be achieved at relatively low temperatures (400 °C for Cu, 450 °C for Ag) and in short time (5 min).

5. Conclusion

Fast metal outward transport in the alternating metal/ceramic NMLs has been successfully provoked and directed for fabricating patterned surface nanostructures, by combining fs laser irradiation with subsequent low temperature post-annealing. By introducing ultrafast laser pulses,

the local microstructure and residual stress state in the NML can be modified along the laser paths. The activation barriers for vacancy formation and migration in the confined metal can thus be reduced locally within the laser-affected zone. Metal outflow can therefore occur at relatively low temperatures within short times (400 °C for Cu/AlN NMLs and 450 °C for Ag/AlN NMLs, 5 min). Surface wire structures can be fabricated in Cu/AlN NMLs, while nanoparticles chains are typically formed in Ag/AlN NMLs. The internal metal contribution to surface nanostructures formation can be precisely located to a few top nanolayers in the NML stack, while preserving the NML structure at larger depths. In-plane and outward metal transport during annealing is accompanied by a bending of the AlN top barrier, and the upper and lower AlN barriers may sinter under the acting capillary forces. Precise laser materials modification on NMLs can localize, accelerate and direct metal transport in such nanoconfined systems, as assisted by a controlled annealing process. Patterned surface nanostructures can thus be achieved with high flexibility. This laser directed mass transport in confinement can be promising for controlling materials behavior at small scales, which may be exploited for fast and pointed nanojoining processes in device integration at small scales or for functional surface nanostructures fabrication for optical or electrical applications.

Associated content

Supporting information

The supporting information is available free of charge via the Internet at <http://pubs.acs.org>.

Supplementary note, TEM images of NMLs, SEM and EDS of as deposited and thermal annealed NMLs, STEM and EDX of thermal annealed NMLs

Corresponding author

*Email: luchan.lin@empa.ch, liulei@tsinghua.edu.cn

Acknowledgment

This work was supported by National Key Research and Development Program of China (2017YFB1104900), and National Natural Science Foundation of China (51520105007, 51775299). L. Lin would like to thank the support from the European Union's Horizon 2020 research and innovation programme under the Marie Skłodowska-Curie grant agreement number 754364. Dr. M. Chiodi is acknowledged for providing nano-multiple-layer samples. Fruitful discussion with Dr. Yeliz Unutulmazsoy and Dr. Bastian Rheingans is appreciated.

Reference

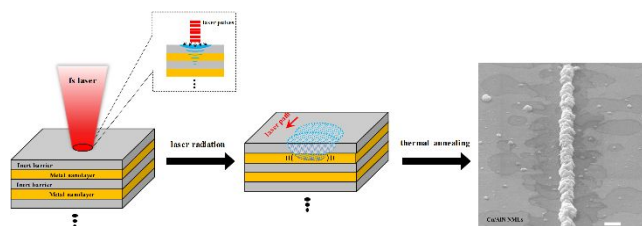
- [1] Yang, J.J.; Pickett, M.D.; Li, X.; Ohlberg, D.A.; Stewart, D.R.; Williams, R.S. Memristive switching mechanism for metal/oxide/metal nanodevices. *Nat. Nanotechn.* **2008**, 3, 429.
- [2] Chaar, L.E.I.; Lamont, L.A.; Zein, N.E.I. Review of photovoltaic technologies. *Renew. Sust. Energ. Rev.* **2011**, 15, 2165.
- [3] Macleod, H.A. Thin-film optical filters. CRC press, **2010**.
- [4] Yang, S.M.; Lee, S.; Jian, J.; Zhang, W.; Lu, P.; Jia, Q.; Wang, H.; Noh, T.W.; Kalinin, S.V.; MacManus-Driscoll, J.L. Strongly enhanced oxygen ion transport through samarium-doped CeO₂ nanopillars in nanocomposite films. *Nat. Commun.* **2015**, 6, 8588.
- [5] Moszner, F.; Cancellieri, C.; Becker, C.; Chiodi, M.; Janczak-Rusch, J.; Jeurgens, L.P.H. Nano-structured Cu/W brazing fillers for advanced joining applications. *J. Mater. Sci. Eng. B* **2016**, 6, 226.
- [6] Shimatsu, T.; Uomoto, M. Atomic diffusion bonding of wafers with thin nanocrystalline metal films. *J. Vac. Sci. Technol. B* **2010**, 28, 706.
- [7] Ding, G.; Clavero, C.; Schweigert, D.; Le, M. Thickness and microstructure effects in the optical and electrical properties of silver thin films. *AIP advances* **2015**, 5, 117234.
- [8] Yao, J.K.; Lin, J.M.; Ye, F.; Fan, P. Optical and electrical properties of transparent conductive air-stable C-axis aligned crystalline InGaZnON thin films. *Opt. Mater. Express* **2018**, 8, 2991.
- [9] Kovalenko, O.; Szabó, S.; Klinger, L.; Rabkin, E. Solid state dewetting of polycrystalline Mo film on sapphire. *Acta Mater.* **2017**, 139, 51-61.
- [10] Kosinova, A.; Kovalenko, O.; Klinger, L.; Rabkin, E. Mechanisms of solid-state dewetting of thin Au films in different annealing atmosphere. *Acta Mater.* **2015**, 83, 91-101.

- [11] Niekiet, F.; Kraschewski, S.; Schweizer, P.; Butz, B.; Spiecker, E. Texture evolution and microstructural changes during solid-state dewetting: a correlative study by complementary in situ TEM techniques. *Acta Mater.* **2016**, 115, 230-241.
- [12] Wejrzanowski, T.; Lewandowska, M.; Sikorshi, K.; Kurzydowski, K. J. Effect of grain size on the melting point of confined thin aluminum films. *J. Appl. Phys.* **2014**, 116, 164302.
- [13] Guo, C.; Pei, Z.; Fan, D.; Liu, R.; Gong, J.; Sun, C. Predicting multilayer film's residual stress from its monolayers. *Mater. Design.* **2016**, 110, 858-864.
- [14] Guo, Q.; Wan, L.; Yu, X.; Vogel, F.; Thompson, G. Influence of phase stability on the in situ growth stresses in Cu/Nb multilayered films, *Acta Mater.* **2017**, 132, 149-161.
- [15] Moszner, F.; Cancellieri, C.; Chiodi, M.; Yoon, S.; Ariosa, D.; Janczak-Rusch, J.; Jeurgens, L.P.H. Thermal stability of Cu/W nano-multilayers. *Acta Mater.* **2016**, 107, 345-353.
- [16] Kumar, A.; Barda, H.; Klinger, L.; Finnis, M. W.; Lordi, V.; Rabkin, E.; Srolovitz, D. J. Anomalous diffusion along metal/ceramic interfaces. *Nat. Commun.* **2018**, 9, 5251.
- [17] Kosinova, A.; Wang, D.; Schaaf, P.; Sharma, A.; Klinger, L.; Rabkin, E. Whiskers growth in thin passivated Au films. *Acta Mater.* **2018**, 149, 154-163.
- [18] Chiodi, M.; Cancellieri, C.; Moszner, F.; Andrzejczuk, M.; Janczak-Rusch, J.; Jeurgens, L.P.H. Massive Ag migration through metal/ceramic nanomultilayers: an interplay between temperature, stress-relaxation and oxygen-enhanced mass transport. *J. Mater. Chem. C* **2016**, 4, 4927.
- [19] Han, H.; Park, J.; Nam, S.; Kim, K.; Choi, G.; Parkin, S.; Jang, H.; Irvine, J. Lattice strain-enhanced exsolution of nanoparticles in thin films. *Nat. Commun.* **2019**, 10, 1471.
- [20] Araullo-Peters, V.; Cancellieri, C.; Chiodi, M.; Janczak-Rusch, J.; Jeurgens, L.P.H. Tailoring fast directional mass transportation of nano-confined Ag-Cu alloys upon heating: effect of the AlN barrier thickness. *ACS Appl. Mater. Interfaces* **2019**, 11, 6605-6614.
- [21] Sutton, A.P.; Balluffi, R. W. Interfaces in crystalline materials. Oxford Science Publications, **1996**.
- [22] Ovid'ko, I.A.; Sheinerman, A.G. Grain-boundary dislocations and enhanced diffusion in nanocrystalline bulk materials and films. *Philos. Mag.* **2003**, 83, 1551.
- [23] Lin, L.; Jeurgens, L.P.H. Local deformation controlled fast directional metal outflow in metal/ceramic nanolayer sandwiches upon low temperature annealing. *ACS Appl. Mater. Interfaces* **2019**, doi.org/10.1021/acsami.9b10498
- [24] Abbott, W.; Corbett, S.; Cunningham, G.; Petford-Long, A.; Zhang, S.; Donegan, J.; McCloskey, D. Solid state dewetting of thin plasmonic films under focused cw-laser irradiation. *Acta Mater.* **2018**, 145, 210-219.

- [25] Lin, L.; Liu, L.; Musselman, K.; Zou, G.; Duley, W.W.; Zhou, Y.N. Plasmonic-radiation-enhanced metal oxide nanowire heterojunctions for controllable multilevel memory. *Adv. Funct. Mater.* **2016**, 26, 5979.
- [26] Lin, L.; Zou, G.; Liu, L.; Duley, W.W.; Zhou, Y.N. Plasmonic engineering of metal-oxide nanowire heterojunctions in integrated nanowire rectification units. *Appl. Phys. Lett.* **2016**, 108, 203107.
- [27] Romashevskiy, S.A.; Tsygankov, P.A.; Ashitkov, S.I.; Agranat, M.B. Layer-by-layer modification of thin-film metal-semiconductor multilayers with ultrafast laser pulses. *Appl. Phys. A* **2018**, 124, 376.
- [28] Fabbro, R.; Peyre, P.; Berthe, L.; Scherpereel, X. Physics and applications of laser-shock processing. *J. Laser Appl.* **1998**, 10, 265.
- [29] Montross, C.S.; Wei, T.; Ye, L.; Clark, G.; Mai, Y. Laser shock processing and its effects on microstructure and properties of metal alloys: a review. *Int. J. Fatigue* **2002**, 24, 1021.
- [30] Janczak-Rusch, J.; Chiodi, M.; Cancellieri, C.; Moszner, F.; Hauert, R.; Pigozzi, G.; Jeurgens, L.P.H. Structural evolution of Ag-Cu nano-alloys confined between AlN nanolayers upon fast heating. *Phys. Chem. Chem. Phys.* **2015**, 17, 28228.
- [31] John, P.B.; Christy, R.W. Optical constants of the noble metals. *Phys. Rev. B* **1972**, 6, 4370-4379.
- [32] Pastrňák, J.; Roskocová, L. Refraction index measurements on AlN single crystals. *Phys. Stat. Sol.* **1966**, 14, K5-K8.
- [33] Gazit, N.; Richter, G.; Sharma, A.; Klinger, L.; Rabkin, E. Engineering of hollow AlAu₂ nanoparticles on sapphire by solid state dewetting and oxidation of Al. *Mater. Design* **2019**, 165, 107557.
- [34] Klinger, L.; Kraft, O.; Rabkin, E. A model of Kirkendall hollowing of core-shell nanowires and nanoparticles controlled by short-circuit diffusion. *Acta Mater.* **2015**, 83, 180-186.
- [35] Jiao, Z.; Sivayoganathan, M.; Duley, W.; He, P.; Zhou, Y. Formation and characterization of femtosecond laser induced subcluster segregated nanoalloys. *J. Phys. Chem. C* **2014**, 118, 24746-24751.
- [36] Hieke, S.W.; Dehm, G.; Scheu, C. Annealing induced void formation in epitaxial Al thin films on sapphire (α -Al₂O₃). *Acta Mater.* **2017**, 140, 355.
- [37] Chen, C.; Nagao, S.; Jiu, J.; Zhang, H.; Sugahara, T.; Suganuma, K. Dry-growth of silver single-crystal nanowires from porous Ag structure. *Appl. Phys. Lett.* **2016**, 108, 263105.
- [38] Floro, J.A.; Chason, E.; Cammarata, R.C.; Srolovitz, D.J. Physical origin of intrinsic stresses in Volmer-Weber thin films. *MRS Bull.* **2002**, 27, 19-25.
- [39] Peyre, P.; Berthe, L.; Scherpereel, X.; Fabbro, R. Laser-shock processing of aluminum-coated 55C1 steel in water-confinement regime, characterization and application to high-cycle fatigue behavior. *J. Mater. Sci.* **1998**, 33, 1421.

- [40] Matsuda, T.; Sano, T.; Arakawa, K.; Hirose, A. Dislocation structure produced by an ultrashort shock pulse. *J. Appl. Phys.* **2014**, 116, 183506.
- [41] Titus, M.S.; Echlin, M.P.; Gumbsch, P.; Pollock, T.M. Dislocation injection in strontium titanate by femtosecond laser pulses. *J. Appl. Phys.* **2015**, 118, 075901.
- [42] Maier, S. *Plasmonics: fundamentals and applications*. Springer Science & Business Media, **2007**.
- [43] Herrmann, L.; Valev, V.; Tserkezis, C.; Barnard, J.; Kasera, S.; Scherman, O.; Aizpurua, J.; Baumberg, J. Threading plasmonic nanoparticles strings with light. *Nat. Commun.* **2014**, 5, 4568.
- [44] Kautek, W.; Rudolph, P.; Daminelli, G.; Krüger, J. Physico-chemical aspects of femtosecond-laser-induced surface nanostructures. *Appl. Phys, A* **2005**, 81, 65-70.
- [45] Qiu, T.; Juhasz, T.; Suarez, C.; Bron, W.; Tien, C. Femtosecond laser heating of multi-layer metals-II. Experiments. *Int. J. Heat Mass Transf.* **1994**, 37, 2799-2808.
- [46] Peruško, D.; Kovač, J.; Petrović, S.; Obradović, M.; Mitrić, M.; Pavlović, V.; Salatić, B.; Jakša, G.; Ciganović, J.; Milosavljević, M. Selective Al-Ti reactivity in laser-processed Al/Ti multilayers. *Mater. Manuf. Processes* **2017**, 32, 1622.
- [47] Choi, I.; Jeong, H.Y.; Shin, H.; Kang, G.; Byun, M.; Kim, H.; Chitu, A.M.; Im, J.S.; Ruoff, R.S.; Choi, S.; et al. Laser-induced phase separation of silicon carbide. *Nat. Commun.* **2016**, 7, 13562.
- [48] Nakajima, T.; Tsuchiya, T.; Kumagai, T. Pulsed laser-induced oxygen deficiency at TiO₂ surface: anomalous structure and electrical transport properties. *J. Solid State Chem.* **2009**, 182, 2560-2565.

TOC Graphic



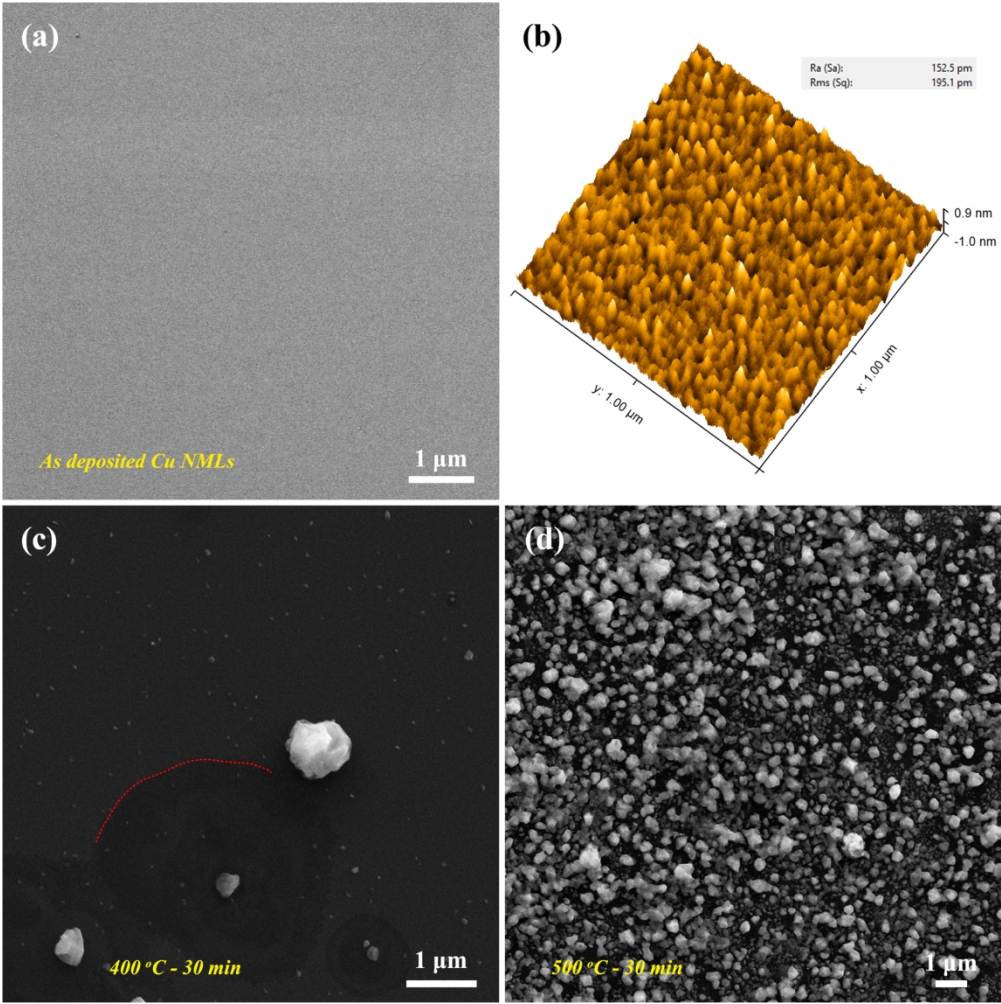


Figure 1. Surface structures of as deposited and thermally annealed [Cu5nm/AlN5nm]*10 NMLs. SEM images of (a) as deposited and thermally annealed NMLs at (c) 400 °C and (d) 500 °C for 30 min in air. (b) AFM topography of as deposited NMLs. Inset in (b) shows the surface roughness of the NML. The dashed line in (c) indicates the boundary of local contrast difference in the SEM image.

186x186mm (300 x 300 DPI)

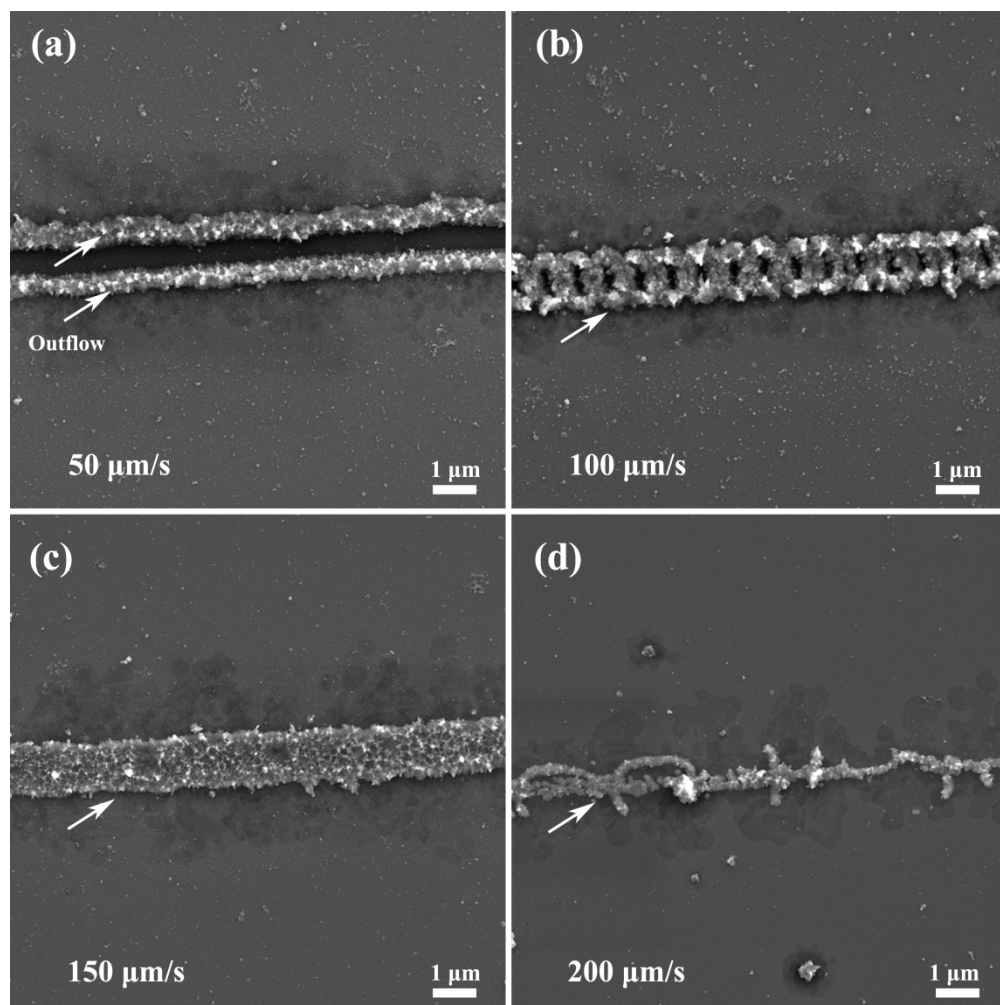


Figure 2. Surface structures formed on [Cu5nm/AlN5nm]*10 NMLs after laser irradiation and subsequent thermal annealing. Laser scanning speed: (a) 50 $\mu\text{m/s}$, (b) 100 $\mu\text{m/s}$, (c) 150 $\mu\text{m/s}$, and (d) 200 $\mu\text{m/s}$. Laser fluence: $\sim 90 \text{ J/cm}^2$. Annealing temperature: 360 $^\circ\text{C}$. Holding time: 5 min. Arrows indicate the surface nanostructures (outflow) after thermal annealing.

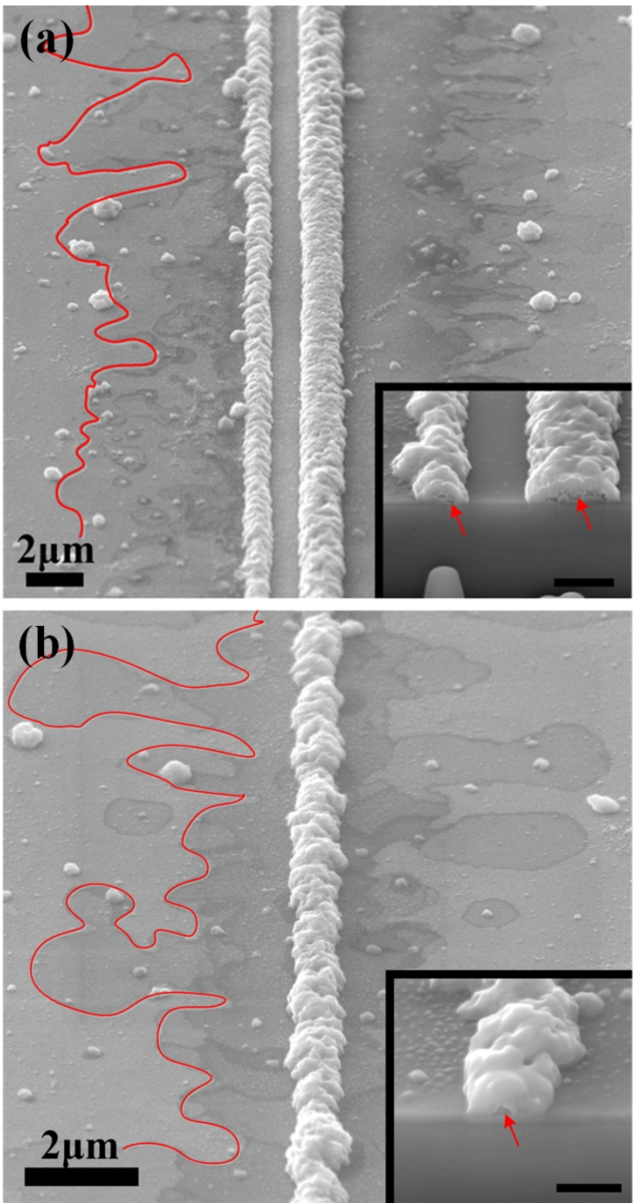


Figure 3. Surface and cross sectional structures of [Cu5nm/AlN5nm]*10 NMLs after laser irradiation and subsequent thermal annealing. Laser fluence: (a) ~55 J/cm² and (b) ~33 J/cm². Scanning speed: 50 μm/s. Annealing temperature: 400 °C. Holding time: 5 min. Red lines sketch the dark contrast regions adjacent to the wires structures. Inset scale bars: (a) 1 μm, (b) 500 nm. Title angle: 45°. Red arrows show the voids in the formed surface structures.

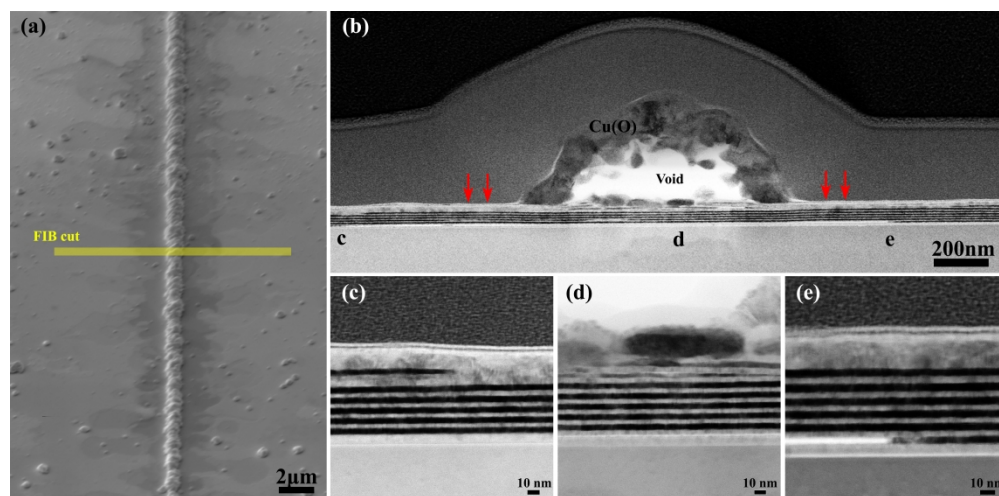


Figure 4. (a) SEM and (b)-(e) BF-STEM images of fs laser irradiated [Cu5nm/AlN5nm]*10 NMLs after thermal annealing at 400 oC for 5 min in air. Laser fluence: ~ 40 J/cm². Scanning speed: 50 μ m/s.

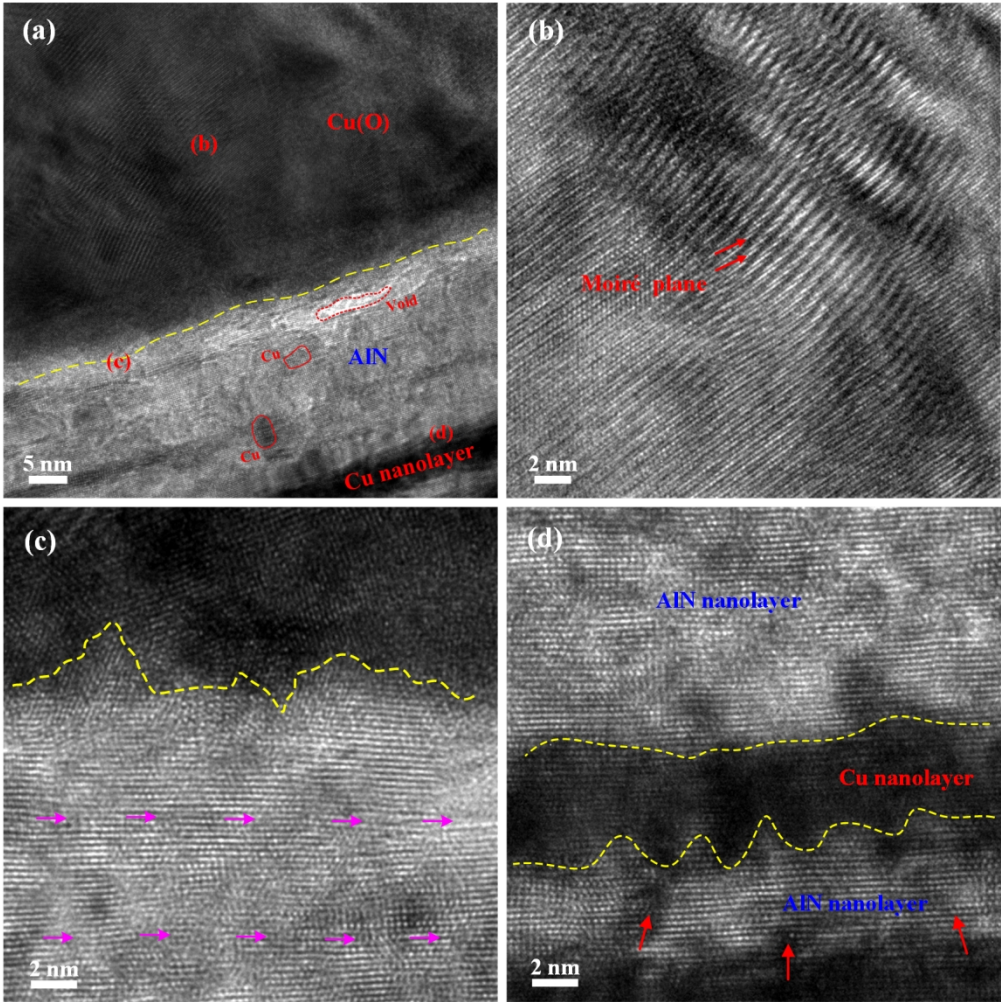


Figure 5. (a) Cross sectional TEM images of the fabricated surface wire on the Cu/AlN NML as indicated in figure 4(b). Yellow dashed lines sketch the Cu-AlN interfaces. HRTEM images of (b) the fabricated surface nanostructure, (c) interfacial state between the surface nanostructure and the NML, and (d) NML after metal migration on the top layers. Pink single arrows in (c) show the estimated boundaries between the as deposited 5 nm AlN nanolayers. Red arrows in (d) show the penetrated Cu in AlN layers.

145x145mm (300 x 300 DPI)

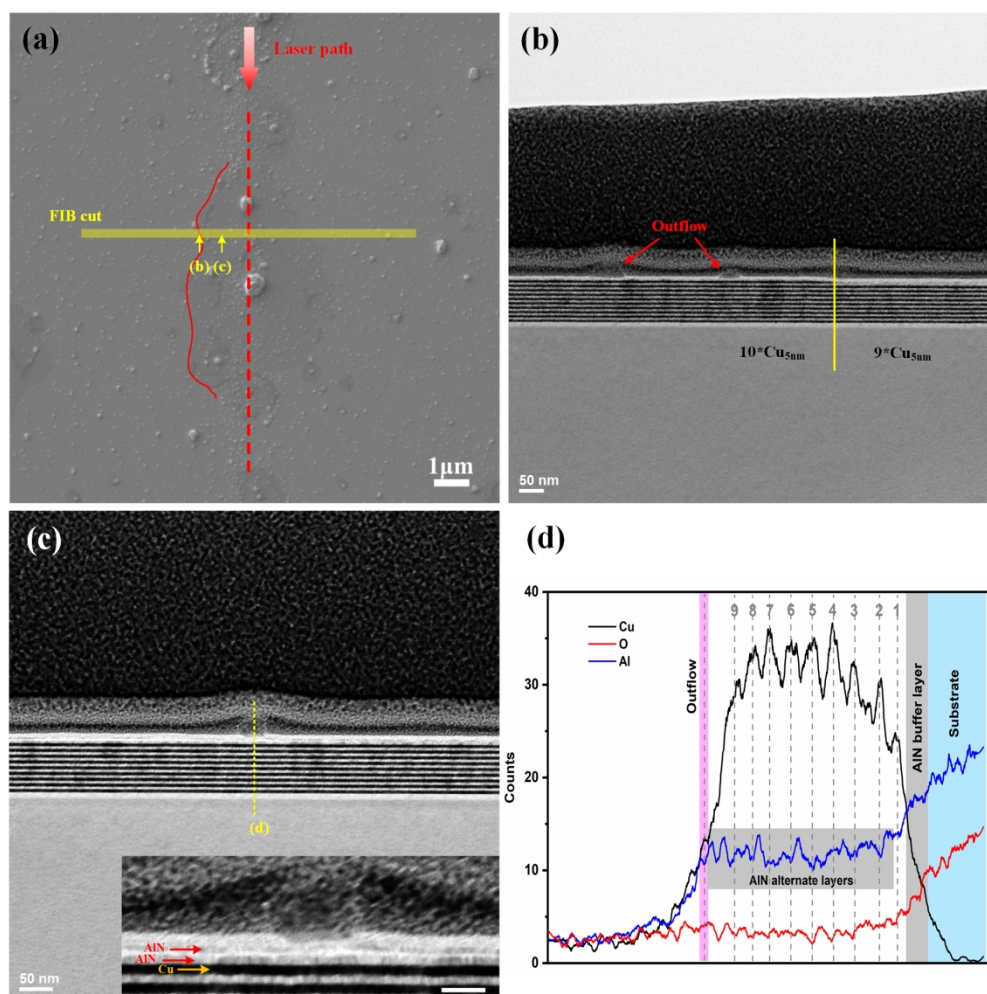


Figure 6. (a) SEM and (b, c) BF-STEM images of fs laser irradiated [Cu5nm/AIN5nm]*10 NMLs after thermal annealing at 400 oC for 5 min in air. (d): EDX elements distribution along the dash line in (c). Laser fluence: ~33 J/cm². Scanning speed: 500 μm/s. Insets scale bar in (c): 20 nm.

173x171mm (300 x 300 DPI)

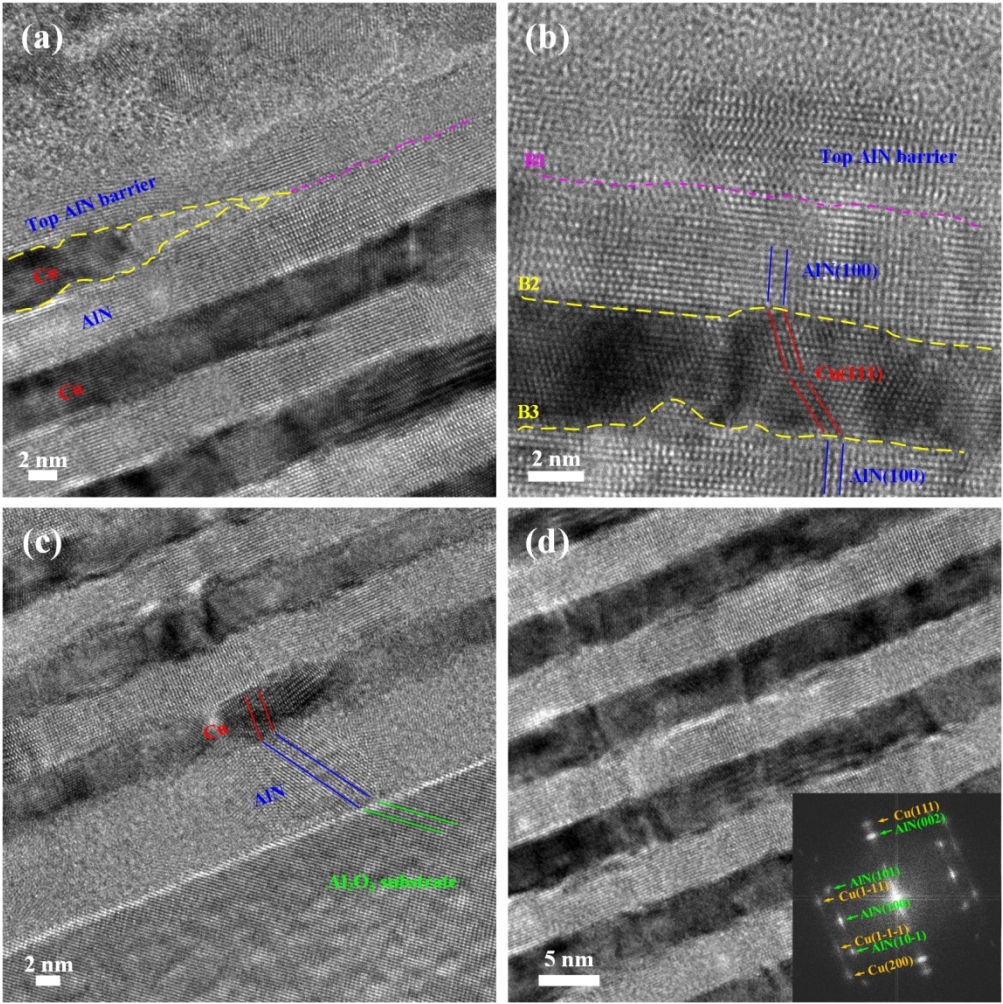


Figure 7. Cross sectional TEM images of laser irradiated [Cu5nm/AlN5nm]*10 NMLs after thermal annealing at 400 oC for 5 min in air. (a)(b): Top. (c): Bottom and (d): Middle.

146x145mm (300 x 300 DPI)

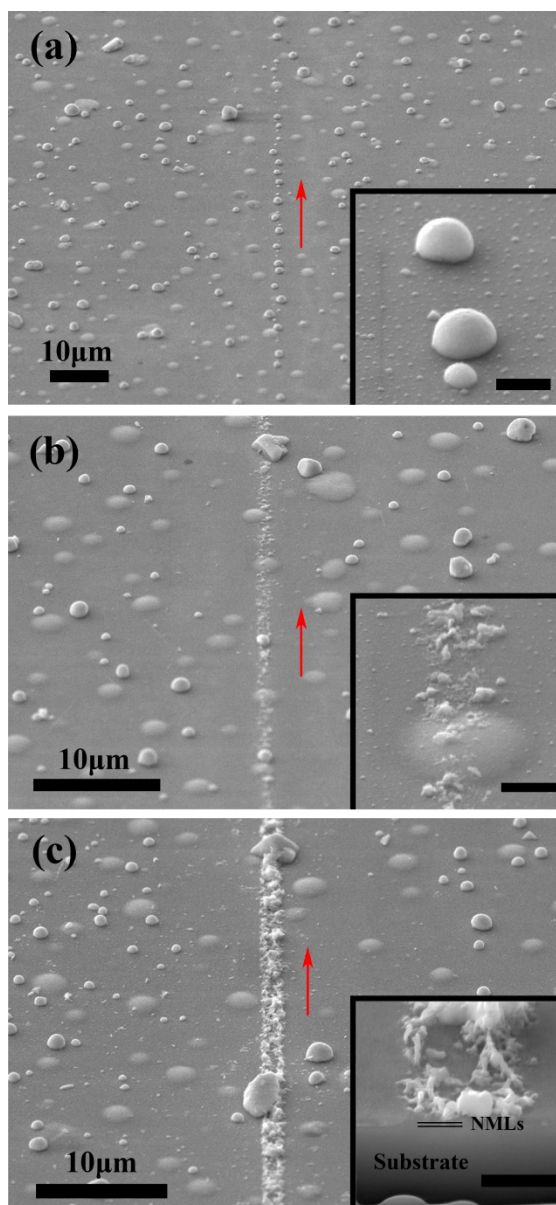


Figure 8. Surface structures of laser irradiated [Ag5nm/AlN5nm]*10 NMLs after subsequent thermal annealing. Scanning speed: (a) 500 $\mu\text{m/s}$, (b) 300 $\mu\text{m/s}$ and (c) 200 $\mu\text{m/s}$. Laser fluence: $\sim 33 \text{ J/cm}^2$. Temperature: 450 oC. Duration: 5 min. Atmosphere: air. Tilt angle: 45°. Inset scale bar: 1 μm .

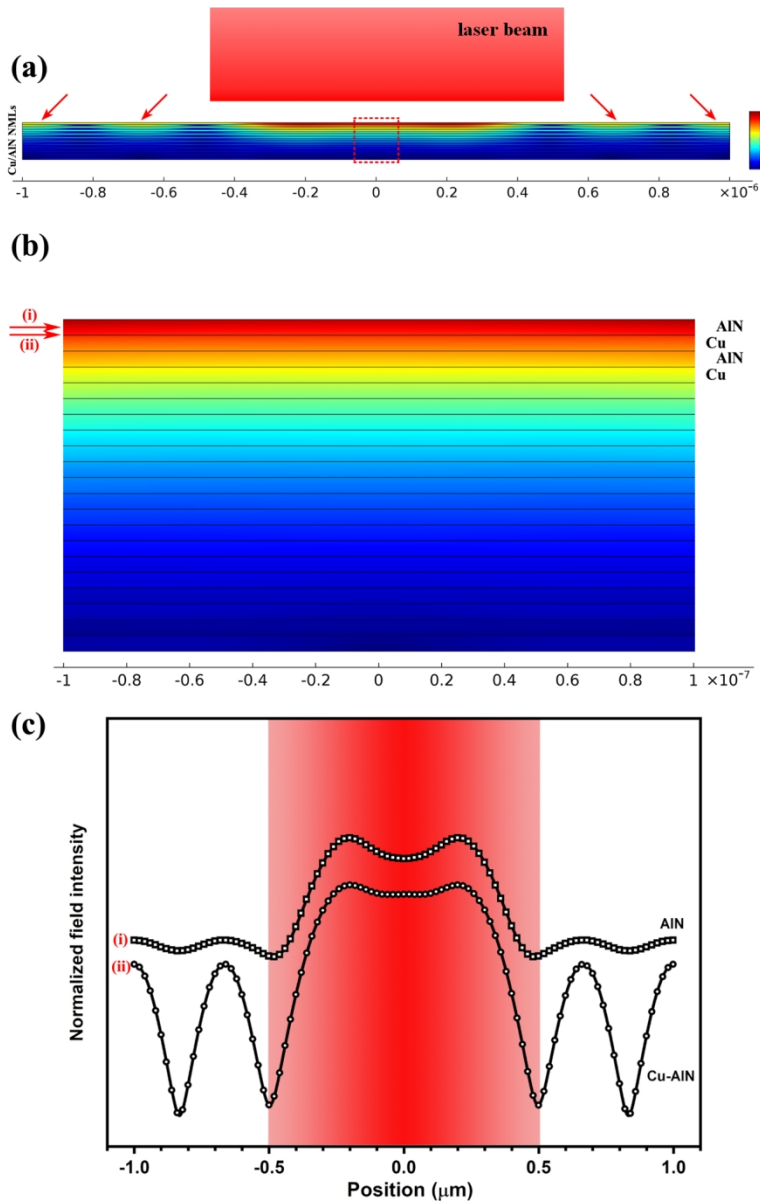


Figure 9. Simulated electric field intensity distribution in [Cu/AlN]*10 NMLs. (a) Field distribution in and out of laser irradiated region. Arrows show the locations with enhanced field intensity outside the laser irradiated region. (b) Field intensity distribution in the rectangle zone in (a). (c) Normalized field intensity along the first AlN layer and Cu-AlN interface on the top. Incident laser beam diameter is 1 μm .

111x174mm (300 x 300 DPI)